ACS APPLIED MATERIALS & INTERFACES

Research Article

www.acsami.org

Rapid Anisotropic Photoconductive Response of ZnO-Coated Aligned Carbon Nanotube Sheets

Jong G. Ok,*[,†,‡] Jae Yong Lee,[‡] Hyoung Won Baac,[‡] Sameh H. Tawfick,[†] L. Jay Guo,[†,‡] and A. John Hart*[,†,§]

[†]Department of Mechanical Engineering and [‡]Department of Electrical Engineering and Computer Science, University of Michigan, Ann Arbor, Michigan 48109, United States

[§]Department of Mechanical Engineering, Massachusetts Institute of Technology, Cambridge, Massachusetts 02139, United States

Supporting Information

ABSTRACT: We investigate the rapid and anisotropic UV-induced photoconductive response of hybrid thin films comprising zinc oxide (ZnO) nanowires (NWs) directly grown on horizontally aligned (HA-) carbon nanotube (CNT) sheets. The films exhibit anisotropic photoconductivity; along the CNTs, conductivity is dominated by the CNTs and the photoconductive gain is lower, whereas perpendicular to the CNTs the photoconductive gain is higher because transport is influenced by ZnO nanoclusters bridging CNT-CNT contacts. Because of the distributed electrical contact provided by the large number of ZnO NWs on top of the HACNT film, this hybrid nanoarchitecture has a significantly greater photocurrent than reported for single ZnO NW-based devices at comparable UV illumination intensity. Moreover, the hybrid architecture where a thin basal film of ZnO ohmically contacts metallic CNTs enables rapid transport of photogenerated electrons from ZnO to CNTs, resulting in sub-second photoresponse upon pulsed illumination. The built-in potential generated across ZnO−CNT heterojunctions competes with the externally applied bias to control the photocurrent amplitude and direction. By tuning the anisotropic conductivity of the CNT network and the morphology of the ZnO or potentially other nanostructured coatings, this material architecture may be engineered in the future to realize high-performance optical and chemical sensors.

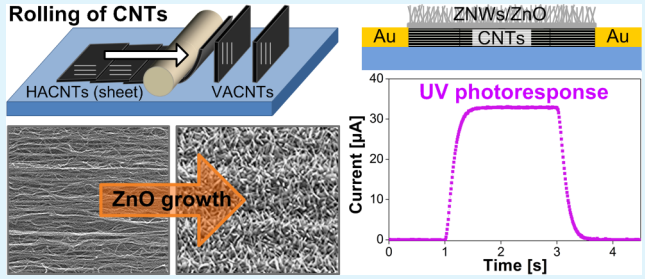

KEYWORDS: *zinc oxide, nanowire, carbon nanotube, hybrid material, photoconductivity, anisotropy*

INTRODUCTION

The fundamental properties of many individual nanostructures such as carbon nanotubes (CNTs)[1] and semiconducting nanowires (NWs)[2] are now well-established; however, methods for both fabrication and characterization of hierarchical assemblies of nanostructures remain relatively nascent. While the integration of NWs and NTs with semiconductor device fabrication demands placement of individual nanostructures, many other applications will rely more on growth and printing techniques that are compatible with large-area and/or flexible substrates.[3,4] Moreover, means for externally-directed and self-directed assembly of elongated nanostructures into aligned films, fibers, and three-dimensional (3D) surfaces, provide opportunity to engineer and study new materials having anisotropic properties.

Specifically, zinc oxide (ZnO) NWs exhibit UV-induced photoelectric characteristics and therefore have been studied for potential use in photodetectors and light emitters.[5−9] Also, the sensitivity of ZnO properties to surface effects has enabled a variety of chemical and biological sensors,[10−14] such as gas sensors that rely on modulation of ZnO conductivity by interaction with the oxygen molecules on the ZnO surface.[12] However, because ZnO and other useful NWs are typically grown on surfaces having low electrical conductivity, post-processing steps such as harvesting, nanopositioning, and/or metallization are often required for device integration.

One attractive strategy to build macroscopic nanoarchitectures is to directly fabricate nanostructures such as ZnO NWs on conductive frameworks.[15] This enables electrical contact to a large number of nanostructures in parallel. Moreover, use of many NWs enables the signal intensity to exceed ambient noise levels, simplifying electrical readout. In particular, CNTs are an attractive framework for 3D NW growth because of their electrical conductivity,[16] chemical robustness,[17] and mechanical strength and flexibility.[18−20] CNTs can be manipulated after synthesis to form horizontally-aligned (HA) CNT sheets,[21] 3D microarchitectures,[22] or long yarns.[23] Moreover, it has been shown that ZnO NWs (herein abbreviated ZNWs) can be directly grown on CNTs via a low-temperature vapor-solid (VS) growth mechanism, where Zn is supplied by evaporation

Received: September 22, 2013
Accepted: December 16, 2013
Published: December 16, 2013

   dx.doi.org/10.1021/am404131r | ACS Appl. Mater. Interfaces 2014, 6, 874−881

of a foil at 500−600 °C.[7,24] This process has been used to build hybrid 3D architectures comprising ZNWs on CNTs configured in vertically-aligned (VA-) forests and HA-sheets fabricated by mechanical rolling of patterned VACNT forests.

Here, we investigate the unique electrical and photoelectric properties of hybrid thin films of ZNWs grown on HACNT sheets. The films exhibit highly anisotropic photoconductivity, governed by the bridging of CNT-CNT contacts by ZnO. The nanoscale proximity of ZnO and CNTs enable sub-second photoresponse upon pulsed illumination as compared to ZnO thin-film photodetectors whose response time can be as long as minutes or more.[25] Moreover, the ZnO−CNT hybrid exhibits a large photocurrent of μA-mA, compared to ~nA levels measured for devices based on a single ZNW[26,27] or ZNW arrays,[28−30] at comparable UV illumination intensity. Last, we study how the amplitude and direction of the photocurrent are controlled by competition between the built-in potential formed in ZnO−CNT interface and the externally applied bias.

RESULTS AND DISCUSSION

Fabrication of ZnO/CNT Hybrid Thin Films. The hybrid film comprising ZNWs directly grown on a HACNT sheet was fabricated via sequential chemical vapor deposition (CVD) processes. First, a multi-wall VACNT "blade" array was grown on Fe catalyst lines (patterned by photolithography) by atmospheric pressure CVD using C_2H_4 as the carbon feedstock.[31] Next, the CNT blades were mechanically rolled and then exposed to a solvent vapor, resulting in a continuous HACNT sheet where the individual blades overlap like toppled dominos (Figure 1a).[21] Then, ZNWs were grown on this HACNT sheet (Figure 1b) via a low-pressure CVD method using Zn foil as the source of Zn vapor.[7,24]

Scanning electron microscopy (SEM) images of the HACNTs before and after ZNW growth are shown in Figures 1c and 1d, respectively. ZNW were formed selectively at high density on the CNTs while few ZNWs were found on the surrounding smooth substrate.[7] This is due to the VS growth mechanism of ZnO, in which a surface roughness is essential to initiate seeding of ZnO nanoclusters.[32] Although oxygen is required to form ZnO from vaporized Zn, it does not degrade the CNTs because the CNTs resist oxidative degradation at the process temperature of 600 °C.

To measure the *I-V* characteristics of the HACNTs and ZNW-CNT hybrids, Au electrodes were deposited at both ends of the HACNT sheet prior to ZNW growth. Before Au deposition, a focused Ion Beam (FIB) was used to cut both ends of the HACNTs, exposing CNT ends down to the substrate (see SEM image in the Supporting Information, Figure S1). Optionally, another Au electrode was deposited in the center area of the film, on top of the ZnO, to characterize the ZnO−CNT heterojunction as discussed later. In this case the CNTs were not cut. Based on the direction of current flow with respect to the alignment of the CNTs in plane (insets to Figure 2), we designate the parallel device as having Au electrodes along the substrate edges perpendicular to the CNTs, and the perpendicular device as having Au electrodes along the edges parallel to the CNTs. Therefore the parallel device was used to measure transport primarily along the CNTs, whereas the perpendicular device was used to measure transport in the direction that is dominated by CNT-CNT junctions.

Anisotropic Electrical and Photoconductive Properties. First, we characterized the direct current (DC) electrical

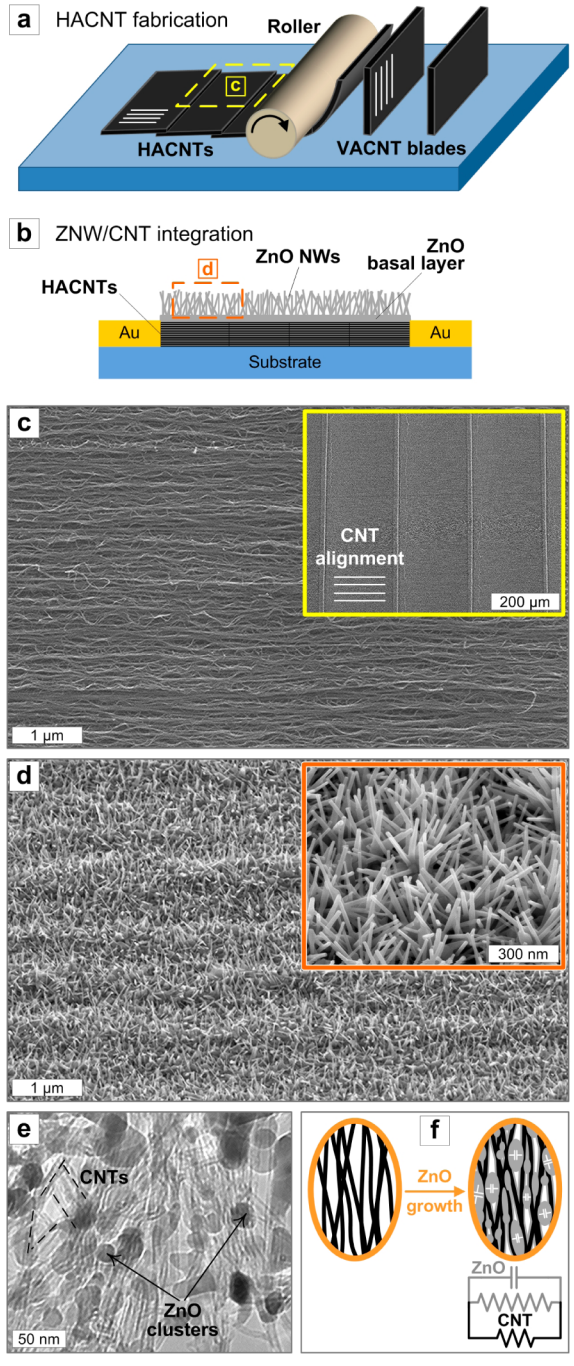

Figure 1. Fabrication of ZnO/CNT hybrid thin films. (a) Mechanical rolling process used to transform the vertically aligned CNT (VACNT) blades into a horizontally aligned CNT (HACNT) sheet, which is the substrate for subsequent ZnO NW (ZNW) growth. (b) Side view schematic of the electrically integrated hybrid sheet; Au electrodes are deposited on both ends of HACNTs prior to ZNW integration to define the current flow either along (parallel configuration) or across (perpendicular configuration) the CNT alignment direction. (c) SEM image of bare HACNT sheet; inset shows the low-magnification view. (d) SEM image of ZnO/CNT surface; inset reveals the enlarged view of ZNWs that are randomly oriented with approximately 25−50 nm diameter and 300−500 nm average length. (e) TEM image taken after the initial growth stage where ZnO nanoclusters are formed on the CNTs, bridging them together. (f) Equivalent circuit schematic for the ZnO/CNT hybrid.

dx.doi.org/10.1021/am404131r | ACS Appl. Mater. Interfaces 2014, 6, 874−881

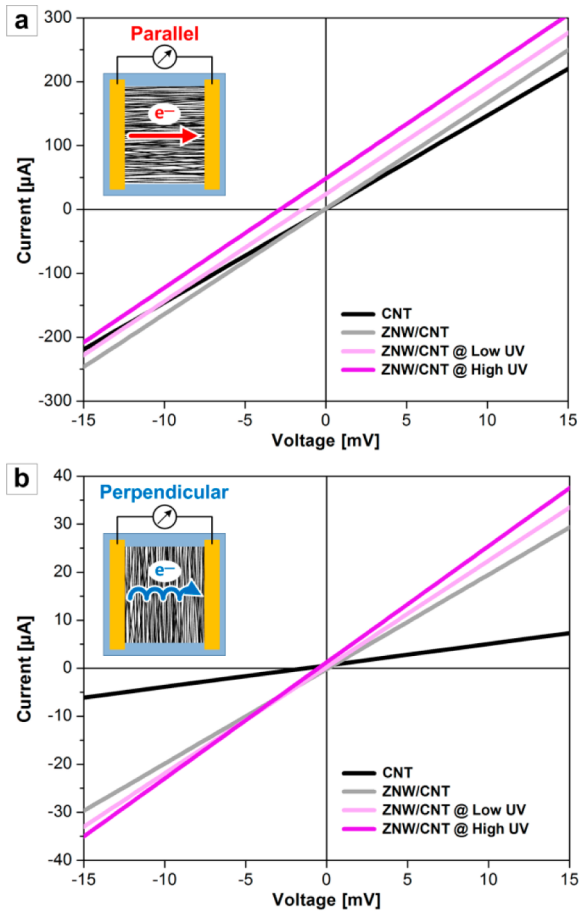

Figure 2. *I*–*V* plots of the ZnO/CNT hybrid films in (a) parallel and (b) perpendicular configurations. The measurements were first performed before and after ZNW growth without UV illumination, indicating the conductivity is improved by the presence of ZnO bridging CNT-CNT contacts. Illumination is continuous UV light with low (1.4 mW/cm^2) and high (7.5 mW/cm^2) power densities.

properties of the ZNW/CNT hybrid films. For both parallel and perpendicular configurations, the device conductivity increases after ZnO growth due to the electrical contribution of the semiconducting ZnO coating on the CNTs.[7] The *I-V* curves measured before and after ZnO growth are shown in Figure 2. The conductivity increase is much greater in the perpendicular direction (340%) than the parallel direction (13%). This anisotropy arises because CNT-CNT junctions dominate transport in the perpendicular direction, and transport in the parallel direction is controlled by the intrinsic conductivity of the long aligned CNTs.

Next, we illuminated the film with UV light (365 nm wavelength) with varied power density to investigate the device photoconductivity and its relation to UV intensity. Here we compared UV power levels of 1.4 mW/cm^2 and 7.5 mW/cm^2. When the device is illuminated with UV light having photon energy exceeding the ZnO bandgap (3.4 eV illumination; 3.37 eV bandgap), an increase in conductivity proportional to UV intensity is observed due to the photogeneration of charge carriers in ZnO. As indicated in Figure 2, this increase is more pronounced in the perpendicular (23 % increase at 7.5 W/cm^2 UV light) than the parallel case (3.5 % increase at 7.5 W/cm^2 UV light). Once again, this is due to the critical role of ZnO in controlling CNT-CNT conduction in the perpendicular configuration, where the ZnO photoconductivity further reduces CNT-CNT contact resistance upon UV illumination.

It has been shown that CNT-CNT conduction is dominated by electron hopping,[33] and we expect that the nanoscale ZnO contacts significantly reduce the contact resistance between the CNTs in the HACNT sheets. Indeed, transmission electron microscopy (TEM) imaging of the ZnO/CNT sample (Figure 1e) where the growth process was halted in less than 1 minute shows that ZnO nanoclusters initially bridge adjacent and contacting CNTs. For longer growth time (typically 20 minutes), additional nucleation proceeds for further connections to form a conformal polycrystalline ZnO coating on the CNT surface, followed by the growth of ZNWs (see Supporting Information, Figure S2, as well as Ok et al.[7]).

Several recent studies have reported photocurrent generation in metal-contacted single-wall CNT (SWNT) films.[34−37] Specifically, Nanot et al. studied the anisotropic photoresponse of substrate-supported SWNT films also made by transformation of vertically grown CNTs, and used scanning photocurrent microscopy to show that the photocurrent results from a gradient in the Seebeck coefficient of CNTs near the contacts.[37] While we cannot rule out the contribution of this effect in our study, and unfortunately were not able to perform further control experiments, we note that our system is fully metallic, comprising MWNTs directly connected to Au electrodes. Moreover, in previous work we found no photoconductive response of our ZnO/CNT hybrids when exposed to UV illumination in vacuum,[7] suggesting dominance of the O_2-mediated photoconduction mechanism as discussed later.

Photoresponse Dynamics. We next investigated the ZnO/CNT photoresponse dynamics by applying pulsed UV illumination. The responses to pulsed illumination (2 second pulse width), in the parallel and perpendicular configurations, are shown in Figures 3a and 3b, respectively. Defining the rise time as that required for the photocurrent to reach 90 % of the peak value, and the decay time as to reach 10% of the peak value,[38] both the rise and decay responses are 0.25−0.35 seconds. Note that this is unusually fast compared to conventional ZnO-based UV photodetectors that are on the orders of a few tens of seconds or more.[5,6,25,39]

The photocurrent response of the ZnO/CNT sheets is attributed to the well-known oxygen-driven electron transfer mechanism for ZnO.[40] In the absence of UV light in ambient, oxygen adsorbs on the ZnO surface and takes a free electron from n-type ZnO to form a chemically adsorbed surface state. When exposed to UV light with energy exceeding the ZnO bandgap, excitons are generated and then separated to electron-hole pairs inside the ZnO. While the holes are trapped on the ZnO surface, the unpaired electrons are free to flow to produce photocurrent. However, the high resistivity of ZnO traditionally results in a high recombination rate and slow dissipation of excess charge carriers, leading to slow response time.[41]

In our ZnO/CNT architecture, the metallic multi-walled CNTs are electrically connected to the thin ZnO layer. Figure 3c illustrates the energy band diagram of the ZnO−CNT system. Under a flat energy band without external bias, the Fermi energy level of ZnO is aligned to that of the CNT because the work function of ZnO (≈5.3 eV[42]) is larger than the work function of CNTs (4.5-5.0 eV[43]). Accordingly, the ZnO−CNT interface is Ohmic and the "built-in" potential is generated in the direction from CNTs to ZnO. Because of this potential slope, the free electrons photogenerated in ZnO conduct readily across the interface and into the CNTs. The

dx.doi.org/10.1021/am404131r | ACS Appl. Mater. Interfaces 2014, 6, 874−881

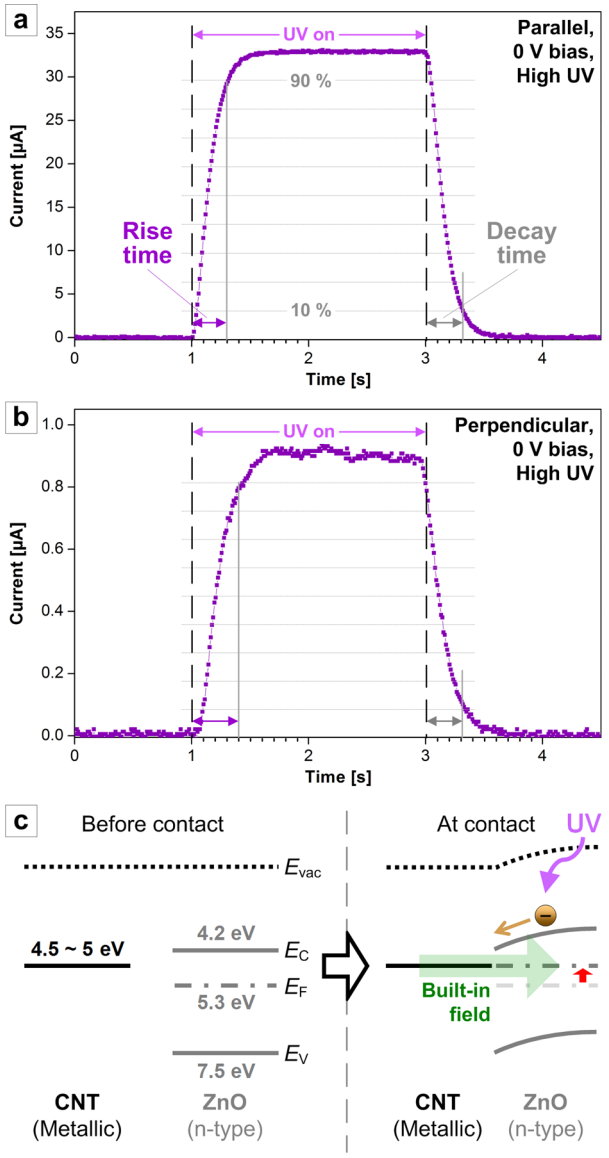

Figure 3. Photoresponse of the ZnO/CNT hybrid film in (a) parallel and (b) perpendicular configurations under a UV pulse (2 seconds, 7.5 mW/cm^2) without external bias. The response time is approximately 0.3 seconds. (c) Band diagrams before (left) and after (right) the contact is formed between ZnO and CNTs, showing that the built-in potential is formed from CNTs to ZnO.

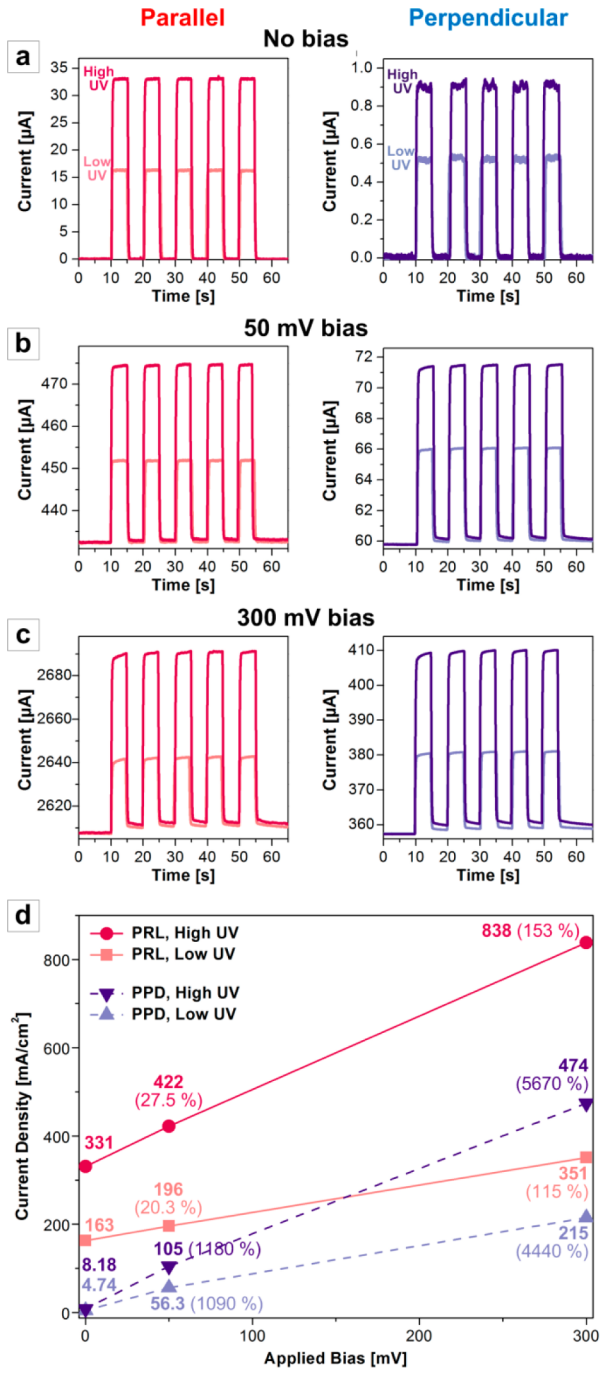

Figure 4. Photocurrent dynamics of ZnO/CNT hybrid films upon pulsed UV illumination under applied biases of (a) 0 V, (b) 50 mV, and (c) 300 mV, for parallel and perpendicular configurations. Each plot shows measurements under high (7.5 mW/cm^2) and low (1.4 mW/cm^2) UV intensities. Plot (d) shows the photocurrent densities calculated per unit surface area, and notes the relative increase (%) to values at 0 V bias.

metallic CNTs improve mobility of these electrons and thus reduce recombination until they are extracted to the external circuit. The thin dimension of the ZnO between CNTs, along with the large interface area, likely also facilitates quick discharge when the UV light is turned off.

Next, using pulsed UV illumination with 5-second duration, we studied the photocurrent behavior as related to the CNT orientation and applied bias voltage (Figure 4). The amplitude of photogenerated current is calculated as the difference between the steady values in the on/off states, as plotted in Figures 4a–c. The corresponding current densities were then calculated per unit cross-section of the HACNT films, and are shown in Figure 4d.

Under UV illumination without any external bias, the ZnO/CNT film behaves like a photovoltaic (PV) cell as it produces photocurrent with no external power source. This supports the transport mechanism of photogenerated electrons from ZnO to CNTs discussed above. When a bias voltage is applied (Figures 4b and 4c), a larger current can be collected at equivalent UV intensity, because the field further increases the electron drift velocity. Also, the photocurrent increases proportionally with respect to the incident UV flux, which can be seen in Figure 4d where the parallel and perpendicular configurations have the same slope under the identical UV intensity. This is consistent

dx.doi.org/10.1021/am404131r | ACS Appl. Mater. Interfaces 2014, 6, 874–881

with an approximation of $I_{ph} \sim V\Phi_{ph}$[44] where I_{ph}, V, and Φ_{ph} are the photocurrent, external bias, and incident photon flux, respectively.

The capacitance of ZnO connecting CNTs in the ZnO/CNT hybrids (see Figure 1f) is responsible for the transient charge-discharge behavior observed in the photocurrent under pulsed illumination, especially under external bias (Figures 4b and 4c). The internally generated bias upon UV illumination charges this ZnO capacitor, and the collective charging behavior of the capacitors limits the rate of response. When the illumination is turned off, the rate of decay is also governed by the discharge rate of the ZnO capacitors. Because the intrinsic ZnO capacitance is proportional to the electric field,[45] this charge-discharge behavior originating from ZnO capacitance becomes larger when the field is increased by external bias.

As shown in Figure 4d, the photocurrent density is greater in the parallel configuration. This is because the higher conductivity along the aligned CNT axis brings about a higher rate of transport of photogenerated charge carriers that are extracted from the ZnO. Consequently more charges are collected, resulting in a larger photocurrent per unit time. Moreover, the relative increase upon illumination is greater in the perpendicular configuration where ZnO has dominant contribution to the total conductivity. This is consistent with the *I-V* sweep results under continuous UV illumination discussed earlier. Owing to these high photocurrents, the hybrid films exhibit high signal-to-noise ratios (SNRs), for example, ~1100 in the parallel and ~30 in the configuration (Figure 4a). Moreover, the measured photocurrent density of the ZnO/CNT hybrid films is significantly higher than those of other ZnO-based photoelectric devices either relying on bare ZnO thin films[46] or using ZNWs but not employing CNTs.[47] We also note that our photocurrents are generated under low-voltage consumption at zero or sub-1 V biases (i.e., 50−300 mV) whereas previous ZnO-based photoelectric structures typically require a few to hundreds of volts.

The external quantum efficiency (EQE), defined as the ratio of the number of electrons photogenerated to the number of incident photons, is typically used to evaluate the performance of photodetectors or PV cells.[48] At 300 mV bias and 1.4 mW/cm^2 illumination, we calculate EQE as high as 36 % for the parallel configuration and 21 % for the perpendicular configuration. The EQE calculation is described in the Supporting Information. These values are already comparable to the previously reported EQEs from other types of nanostructured photodetectors.[48] Interestingly, these EQEs at 300 mV bias decrease to 16% for parallel and 9 % for perpendicular devices under higher UV illumination of 7.5 mW/cm^2, indicating that increased photon flux from more intense UV light is not all linearly converted to free electrons. Also, some photon energy must be dissipated via surface reflection, scattering, and/or thermal loss. Hence, the EQE of hybrid ZnO/CNT photoconductors can be potentially improved by optimizing the structural parameters (e.g., HACNT thickness) and/or by tuning the incident UV intensity.

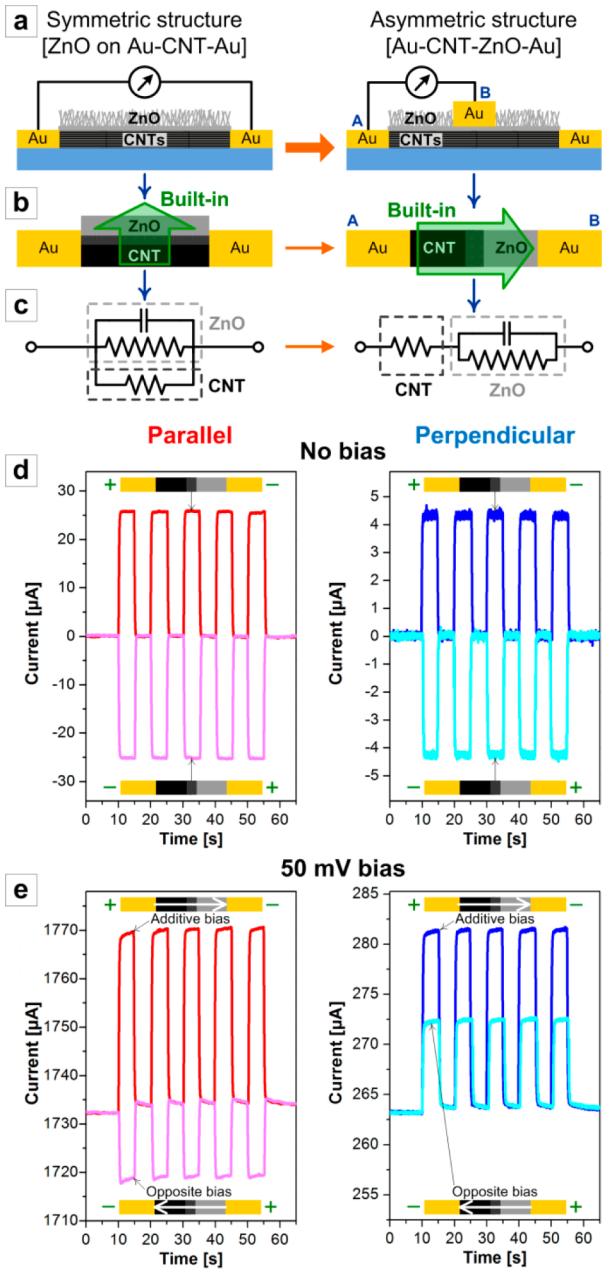

Figure 5. (a) Schematic of asymmetric Au-CNT-ZnO-Au structures starting from the basic ZnO/CNT device (left) by depositing another Au electrode across the middle of the ZnO-coated area (right). The equivalent diagrams of (b) structural schemes with the built-in potential arrows and (c) electrical circuits are illustrated, demonstrating the electrons must flow "through" the ZnO−CNT junctions in the asymmetric device to be collected by the external circuit. Photocurrent measured upon pulsed UV illumination, for asymmetric parallel (left) and perpendicular (right) configurations, with bias of (d) 0 V and (e) 50 mV. The read direction and/or bias direction are described on top or bottom area of each plot for clarification.

Control of Photocurrent Direction. Fabrication of another Au electrode over the middle of the ZnO/CNT hybrid film (i.e., Au-ZnO−CNT-Au, Figure 5a) let us further investigate how the ZnO−CNT junction behavior is controlled by the external bias. Via equivalent circuit diagrams (Figure 5c), we define the "symmetric" configuration (left) when ZnO and CNTs are connected in parallel, and the "asymmetric" configuration (right) when ZnO and CNTs are connected in series. As schematically shown in Figure 5**b**, CNTs carry most current in the symmetric configuration where the built-in potential facilitates electron extraction from ZnO to CNTs, and the external bias plays a main role in carrying electrons. In the asymmetric configuration, the built-in potential directly influences the overall current flow by cooperating or competing

dx.doi.org/10.1021/am404131r | ACS Appl. Mater. Interfaces 2014, 6, 874−881

with the external bias because the ZnO and CNTs are connected in series between the electrodes.

Under the absence of external bias, the photocurrent always flows (25 μA and 5 μA for parallel and perpendicular devices, respectively), from CNTs to ZnO in this asymmetric configuration, and is not influenced by the polarity of the measurement leads (Figure 5d). This is because, without external bias, the built-in field across the ZnO−CNT interface is the only motive to carry electrons to the collecting circuit. However, when external bias is applied, the external bias and the built-in potential cooperate or compete to determine the net photocurrent amplitude and direction. Here we define the "additive" and "opposite" biases as the external fields applied along and against the built-in potential, respectively.

Under additive external bias, a higher photocurrent from CNTs to ZnO is measured for both parallel (∼35 μA) and perpendicular (∼18 μA) devices (upper plots in Figure 5e). This is because the external bias applied in the same direction of the built-in potential helps to build a higher electric field at the ZnO−CNT interface and facilitates further transport of photogenerated electrons from ZnO to CNTs. This cumulative bias effect is independent of the in-plane CNT alignment direction.

On the other hand when the opposite bias is applied, it works against the built-in field, decreasing the net electric field across the ZnO−CNT junction. This reduces the UV-induced photocurrent amplitudes for both parallel (∼15 μA) and perpendicular (∼10 μA) configurations (lower plots in Figure 5e). Interestingly, the net current flow direction under the opposite bias is different in our parallel and perpendicular devices. The net current direction in the parallel case remains unchanged (i.e., from CNTs to ZnO, indicated by the (−) sign with the switched leads). Meanwhile, the current flow is reversed in the perpendicular case (i.e., from ZnO to CNTs, indicated by the same (+) sign of current with the switched leads).

Again, the built-in potential is always formed from CNTs to ZnO, which is constant and independent of the external bias because it is determined by the material properties of ZnO and CNTs. The amount of current driven by this built-in potential is dictated by the system resistance at the interface of the ZnO and CNTs. Therefore, this built-in-driven "one-way" current (i.e., built-in current) will be of much larger magnitude in the parallel configuration because of the lower resistance than for the perpendicular configuration. Under UV illumination, the opposite bias induces the photocurrent to be driven from ZnO to CNTs. These two currents with opposite directions compete with each other to finally determine the net current flow direction.

With increasing opposite bias, we expect there is always a "transition" point of net current direction for each device. For example, under 50 mV external bias, the current drifting along the direction of the external bias is larger than the built-in current in the perpendicular configuration because of its larger intrinsic system resistance. This results in the reversed net current direction. In contrast, the lower resistance of the CNTs in the parallel configuration sustains the current flow direction from CNTs to ZnO under 50 mV bias. However, we expect this direction could be reversed under higher opposite bias. Further experiments will be necessary to confirm this and to find the external bias values at the "transition" point for each device.

Moving forward, it will be important to consider applications that may utilize the anisotropic properties to create sensing devices. One such example is gas sensors that could utilize signals from both parallel and perpendicular directions to increase sensitivity and/or range. Another example could collect the UV-induced photocurrent as a means of power harvesting, and combine photoconductive and chemiresistive effects for sensing. Moreover, this study presents a method for characterizing the unique anisotropic properties of functional thin films supported by aligned CNTs, which can be applied to other oxide and semiconductor nanoarchitectures in future work.

CONCLUSION

In summary, we have studied the rapid and anisotropic photoresponse characteristics of horizontally aligned CNT sheets coated with ZnO. The HACNT film provides a scalable conducting framework which enables thin-film integration of NWs, and the entire process is compatible with standard lithography, printing, and CVD methods. Upon UV illumination, the hybrid ZnO/CNT film shows anisotropic photoconductivity depending on the HACNT alignment, along with fast photoresponse which is attributed to the conformal large-area interface between ZnO and CNTs. We showed that the photocurrent amplitude and direction depend on the alignment and bias direction. By tuning the anisotropic conductivity of the CNT network and the morphology of the ZnO, this material architecture may be engineered in the future for high-performance and low-noise optical and chemical sensors.

METHODS

Fabrication of ZnO/CNT Hybrid Films. The CNT line pattern photomask was designed with a 1.5 × 1.5 cm area, containing an array of 1.5 cm slits with 20 μm width and 200 μm spacing. Catalyst and support layers of Fe (1 nm) and Al_2O_3 (10 nm) were sputtered on a Si wafer with 250 nm of thermal SiO_2 and then were patterned by photolithography. The CNT blades were grown on this catalyst pattern by atmospheric pressure CVD[31] in a single-zone tube furnace (Thermo-Fisher MiniMite) at the set point temperature of 775 °C for 5 minutes, under a mixed flow of 100 sccm He, 400 sccm H_2 (99.999% UHP, Metro Welding), and 100 sccm C_2H_4 (99.9% UHP, Airgas, Inc.). This results in VACNT blades having ∼220 μm average height, allowing sufficient overlap when the CNTs are rolled over (Figures 1a and 1c). The CNT blades were then transformed to HACNT sheets by mechanical rolling followed by elastocapillary densification,[21] resulting in ∼1.5 μm thick HACNTs. Au electrodes (800 nm thick) were deposited by e-beam evaporation on both ends of the HACNT sheet (after etching of the ends by FIB, Supporting Information, Figure S2) using a shadow mask laser-cut in polyester film. Then, ZNWs were directly grown on the HACNT sheet device having Au electrodes (Figures 1b and 1d) by the low-pressure CVD under 17.5/20 sccm air/He mixture flowing at 6 Torr pressure with 600 °C set point temperature using a piece of Zn foil (≈0.6 g, 99.98%, Alfa Aesar) as a source. After a typical 20 minute-long growth, the typical diameter and length of the resulting ZNWs were approximately 25−50 nm and 300−500 nm, respectively. For asymmetric device preparation, an additional Au electrode was deposited in the middle after the ZNW growth process (Figure 5a). A more detailed procedure for photolithography and deposition and full description of CNT and ZNW growth processes can also be found in our previous paper.[7]

Microscopy. A Philips XL30-FEG SEM operating typically at 10 kV was used for SEM imaging. TEM imaging was performed using a JEOL 3011 TEM instrument operating at 300 keV. To prepare the sample for TEM characterization, as-grown CNTs were sonicated in toluene without any surfactant for 1 h and several drops of this dispersion were applied to a copper mesh TEM grid. After drying, the CNT-coated copper grid was then loaded into the ZnO growth process. Approximately 1 minute after the Zn evaporation step began,

the growth process was abruptly stopped by cooling the furnace rapidly under a He purge.

Electrical and Photoelectric Characterization. The measurements of electrical and photoelectric properties of ZnO/CNT devices were conducted using a custom-built 4-point probe station. Illumination was supplied using a UV lamp (Dymax, Model 2000 Flood; 365 nm wavelength, 75 mW/cm^2 at the housing outlet). By adjusting the distance between the UV source and the device, the UV intensity was varied and measured by the power meter. For measuring conductivity (Figure 2), the DC voltage was swept under continuous UV illumination with the current recording. For characterizing the photocurrent generation and photoresponse dynamics (Figures 3–5), a pulsed UV light was illuminated with or without the constant DC bias applied between the electrodes while the current and time were recorded. All UV experiments were carried out in a dark room.

■ ASSOCIATED CONTENT

Supporting Information

Additional SEM images of the CNT structures before and after ZnO NW growth, and details of the EQE calculations. This material is available free of charge via the Internet at http://pubs.acs.org.

■ AUTHOR INFORMATION

Corresponding Authors

*E-mail: jgok@umich.edu (J.G.O.).
*E-mail: ajhart@mit.edu (A.J.H.).

Notes

The authors declare no competing financial interest.

■ ACKNOWLEDGMENTS

This work was funded by the DARPA Microsystems Technology Office through a Young Faculty Award to A.J.H. J.G.O. was supported in part by the National Science Foundation Scalable Nanomanufacturing Program (DMR-1120187). We thank Yongyi Zhang for help with TEM imaging, Sei-Jin Park for shadow mask preparation, and Girish Kulkarni, Nanditha Dissanayake, and Prof. Zhaohui Zhong for use of their electrical testing facilities and assistance with electrical characterization. Electron microscopy was performed at the University of Michigan Electron Microbeam Analysis Laboratory (EMAL). Microfabrication was performed at the University of Michigan Lurie Nanofabrication Facility (LNF), which is a member of the National Nanotechnology Infrastructure Network (NNIN).

■ REFERENCES

(1) Dresselhaus, M. S., Dresselhaus, G., Avouris, P., Eds.; *Carbon Nanotubes: Synthesis, Structure, Properties and Applications*; Springer: New York, 2001.
(2) Fan, H. J.; Werner, P.; Zacharias, M. *Small* **2006**, *2*, 700–717.
(3) Cao, Q.; Kim, H. S.; Pimparkar, N.; Kulkarni, J. P.; Wang, C. J.; Shim, M.; Roy, K.; Alam, M. A.; Rogers, J. A. *Nature* **2008**, *454*, 495–500.
(4) Sun, Y. G.; Rogers, J. A. *Adv. Mater.* **2007**, *19*, 1897–1916.
(5) Kind, H.; Yan, H. Q.; Messer, B.; Law, M.; Yang, P. D. *Adv. Mater.* **2002**, *14*, 158–160.
(6) Soci, C.; Zhang, A.; Xiang, B.; Dayeh, S. A.; Aplin, D. P. R.; Park, J.; Bao, X. Y.; Lo, Y. H.; Wang, D. *Nano Lett.* **2007**, *7*, 1003–1009.
(7) Ok, J. G.; Tawfick, S.; Juggernauth, K.; Sun, K.; Zhang, Y.; Hart, A. J. *Adv. Funct. Mater.* **2010**, *20*, 2470–2480.
(8) Wang, X. D.; Summers, C. J.; Wang, Z. L. *Nano Lett.* **2004**, *4*, 423–426.
(9) Johnson, J. C.; Knutsen, K. P.; Yan, H. Q.; Law, M.; Zhang, Y. F.; Yang, P. D.; Saykally, R. J. *Nano Lett.* **2004**, *4*, 197–204.
(10) Wan, Q.; Li, Q. H.; Chen, Y. J.; Wang, T. H.; He, X. L.; Li, J. P.; Lin, C. L. *Appl. Phys. Lett.* **2004**, *84*, 3654–3656.
(11) Kang, B. S.; Heo, Y. W.; Tien, L. C.; Norton, D. P.; Ren, F.; Gila, B. P.; Pearton, S. J. *Appl. Phys. A: Mater. Sci. Process* **2005**, *80*, 1029–1032.
(12) Wang, J. X.; Sun, X. W.; Yang, Y.; Huang, H.; Lee, Y. C.; Tan, O. K.; Vayssieres, L. *Nanotechnology* **2006**, *17*, 4995–4998.
(13) Ahmad, M.; Pan, C. F.; Luo, Z. X.; Zhu, J. *J. Phys. Chem. C* **2010**, *114*, 9308–9313.
(14) Stafiniak, A.; Boratynski, B.; Baranowska-Korczyc, A.; Szyszka, A.; Ramiaczek-Krasowska, M.; Prazmowska, J.; Fronc, K.; Elbaum, D.; Paszkiewicz, R.; Tlaczala, M. *Sens. Actuators, B* **2011**, *160*, 1413–1418.
(15) Eder, D. *Chem. Rev.* **2010**, *110*, 1348–1385.
(16) Li, H. J.; Lu, W. G.; Li, J. J.; Bai, X. D.; Gu, C. Z. *Phys. Rev. Lett.* **2005**, *95*, 086601.
(17) Sotiropoulou, S.; Chaniotakis, N. A. *Anal. Bioanal. Chem.* **2003**, *375*, 103–105.
(18) Ruoff, R. S.; Lorents, D. C. *Carbon* **1995**, *33*, 925–930.
(19) Gaillard, J.; Skove, M.; Rao, A. M. *Appl. Phys. Lett.* **2005**, *86*, 233109.
(20) Iijima, S.; Brabec, C.; Maiti, A.; Bernholc, J. *J. Chem. Phys.* **1996**, *104*, 2089–2092.
(21) Tawfick, S.; O'Brien, K.; Hart, A. J. *Small* **2009**, *5*, 2467–2473.
(22) De Volder, M.; Tawfick, S. H.; Park, S. J.; Copic, D.; Zhao, Z. Z.; Lu, W.; Hart, A. J. *Adv. Mater.* **2010**, *22*, 4384–4389.
(23) Zhang, M.; Atkinson, K. R.; Baughman, R. H. *Science* **2004**, *306*, 1358–1361.
(24) Wang, K.; Chen, J. J.; Zhou, W. L.; Zhang, Y.; Yan, Y. F.; Pern, J.; Mascarenhas, A. *Adv. Mater.* **2008**, *20*, 3248–3253.
(25) Jin, Y. Z.; Wang, J. P.; Sun, B. Q.; Blakesley, J. C.; Greenham, N. C. *Nano Lett.* **2008**, *8*, 1649–1653.
(26) Heo, Y. W.; Kang, B. S.; Tien, L. C.; Norton, D. P.; Ren, F.; La Roche, J. R.; Pearton, S. J. *Appl. Phys. A: Mater. Sci. Process* **2005**, *80*, 497–499.
(27) Zhang, D.; Lee, S. K.; Chava, S.; Berven, C. A.; Katkanant, V. *Phys. B* **2011**, *406*, 3768–3772.
(28) Keem, K.; Kim, H.; Kim, G. T.; Lee, J. S.; Min, B.; Cho, K.; Sung, M. Y.; Kim, S. *Appl. Phys. Lett.* **2004**, *84*, 4376–4378.
(29) Hsu, C. L.; Chang, S. J.; Lin, Y. R.; Li, P. C.; Lin, T. S.; Tsai, S. Y.; Lu, T. H.; Chen, I. C. *Chem. Phys. Lett.* **2005**, *416*, 75–78.
(30) Li, Y. B.; Della Valle, F.; Simonnet, M.; Yamada, I.; Delaunay, J. J. *Nanotechnology* **2009**, *20*, 045501.
(31) Hart, A. J.; Slocum, A. H. *J. Phys. Chem. B* **2006**, *110*, 8250–8257.
(32) Ho, S. T.; Wang, C. Y.; Liu, H. L.; Lin, H. N. *Chem. Phys. Lett.* **2008**, *463*, 141–144.
(33) Pint, C. L.; Xu, Y. Q.; Morosan, E.; Hauge, R. H. *Appl. Phys. Lett.* **2009**, *94*, 182107.
(34) St-Antoine, B.C.; Menard, D.; Martel, R. *Nano Res.* **2012**, *5*, 73–81.
(35) St-Antoine, B.C.; Menard, D.; Martel, R. *Nano Lett.* **2009**, *9*, 3503–3508.
(36) Omari, M.; Kouklin, N.A. *Appl. Phys. Lett.* **2011**, *98*, 3.
(37) Nanot, S.; Cummings, A. W.; Pint, C. L.; Ikeuchi, A.; Akiho, T.; Sueoka, K.; Hauge, R. H.; Leonard, F.; Kono, J. *Sci. Rep.* **2013**, *3*, 1335.
(38) Yang, P. Y.; Wang, J. L.; Tsai, W. C.; Wang, S. J.; Lin, J. C.; Lee, I. C.; Chang, C. T.; Cheng, H. C. *Thin Solid Films* **2010**, *518*, 7328–7332.
(39) Kim, W.; Chu, K. S. *Phys. Status Solidi A* **2009**, *206*, 179–182.
(40) Takahashi, Y.; Kanamori, M.; Kondoh, A.; Minoura, H.; Ohya, Y. *Jpn. J. Appl. Phys., Part 1* **1994**, *33*, 6611–6615.
(41) Ozgur, U.; Alivov, Y. I.; Liu, C.; Teke, A.; Reshchikov, M. A.; Dogan, S.; Avrutin, V.; Cho, S. J.; Morkoc, H. *J. Appl. Phys.* **2005**, *98*, 041301.
(42) Jo, S. H.; Banerjee, D.; Ren, Z. F. *Appl. Phys. Lett.* **2004**, *85*, 1407–1409.
(43) Ago, H.; Kugler, T.; Cacialli, F.; Salaneck, W. R.; Shaffer, M. S. P.; Windle, A. H.; Friend, R. H. *J. Phys. Chem. B* **1999**, *103*, 8116–8121.

(44) Prades, J. D.; Jimenez-Diaz, R.; Hernandez-Ramirez, F.; Fernandez-Romero, L.; Andreu, T.; Cirera, A.; Romano-Rodriguez, A.; Cornet, A.; Morante, J. R.; Barth, S.; Mathur, S. *J. Phys. Chem. C* **2008**, *112*, 14639−14644.
(45) Tornow, J.; Ellmer, K.; Szarko, J.; Schwarzburg, K. *Thin Solid Films* **2008**, *516*, 7139−7143.
(46) Coppa, B. J.; Fulton, C. C.; Kiesel, S. M.; Davis, R. F.; Pandarinath, C.; Burnette, J. E.; Nemanich, R. J.; Smith, D. J. *J. Appl. Phys.* **2005**, *97*, 103517.
(47) Yang, X. Y.; Wolcott, A.; Wang, G. M.; Sobo, A.; Fitzmorris, R. C.; Qian, F.; Zhang, J. Z.; Li, Y. *Nano Lett.* **2009**, *9*, 2331−2336.
(48) Konstantatos, G.; Sargent, E. H. *Nat. Nanotechnol.* **2010**, *5*, 391−400.